


Analysis of ligand binding and resulting conformational changes in pyrophosphatase NUDT9

Ellen Gattkowski¹, Trevor J. Rutherford², Franziska Möckl³, Andreas Bauche³, Simon Sander¹, Ralf Fliegert³ and Henning Tidow¹ 

¹ The Hamburg Advanced Research Center for Bioorganic Chemistry (HARBOR) & Department of Chemistry, Institute for Biochemistry and Molecular Biology, University of Hamburg, Germany

² MRC Laboratory of Molecular Biology, Cambridge, UK

³ Department of Biochemistry and Molecular Cell Biology, University Medical Centre Hamburg-Eppendorf, Germany

Keywords

ADPR; conformational change; FRET sensor; ligand; pyrophosphatase; TRPM2

Correspondence

H. Tidow, Department of Chemistry, Institute for Biochemistry and Molecular Biology, University of Hamburg, Luruper Chaussee 149, D-22761 Hamburg, Germany
Tel: +49 40428388984
E-mail: tidow@chemie.uni-hamburg.de

(Received 10 April 2021, revised 4 June 2021, accepted 29 June 2021)

doi:10.1111/febs.16097

Nudix hydrolase 9 (NUDT9) is a member of the nucleoside linked to another moiety X (NUDIX) protein superfamily, which hydrolyses a broad spectrum of organic pyrophosphates from metabolic processes. ADP-ribose (ADPR) has been the only known endogenous substrate accepted by NUDT9 so far. The Ca²⁺-permeable transient receptor potential melastatin subfamily 2 (TRPM2) channel contains a homologous NUDT9-homology (NUDT9H) domain and is activated by ADPR. Sustained Ca²⁺ influx via ADPR-activated TRPM2 triggers apoptotic mechanisms. Thus, a precise regulation of cellular ADPR levels by NUDT9 is essential. A detailed characterization of the enzyme-substrate interaction would help to understand the high substrate specificity of NUDT9. Here, we analysed ligand binding to NUDT9 using a variety of biophysical techniques. We identified 2'-deoxy-ADPR as an additional substrate for NUDT9. Similar enzyme kinetics and binding affinities were determined for the two ligands. The high-affinity binding was preserved in NUDT9 containing the mutated NUDIX box derived from the human NUDT9H domain. NMR spectroscopy indicated that ADPR and 2'-deoxy-ADPR bind to the same binding site of NUDT9. Backbone resonance assignment and subsequent molecular docking allowed further characterization of the binding pocket. Substantial conformational changes of NUDT9 upon ligand binding were observed which might allow for the development of NUDT9-based ADPR fluorescence resonance energy transfer sensors that may help with the analysis of ADPR signalling processes in cells in the future.

Introduction

Proteins from the nucleoside linked to another moiety X (NUDIX) superfamily play an important role in all domains of life as they control the levels of metabolic intermediates and signalling molecules of the general structure of a nucleoside diphosphate linked to another moiety X (reviewed in [1]). The

members of this diverse class of proteins share a common sequence motif with the conserved amino acid sequence G_X₅E_X₅[UA]xRE_X₂EE_XGU (where U represents an aliphatic hydrophobic residue) that forms a helix-loop-helix structure [2,3]. Catalysis depends on coordination of divalent cations by the

Abbreviations

ADPR, ADP-ribose; FRET, fluorescence resonance energy transfer; IMAC, immobilized metal affinity chromatography; ITC, isothermal titration calorimetry; NUDIX, nucleoside linked to another moiety X; NUDT9, Nudix hydrolase 9; NUDT9H, NUDT9-homology; SAXS, small-angle X-ray scattering; TEV, tobacco etch virus; TRPM2, transient receptor potential melastatin subfamily 2.

highly conserved glutamate residues in the central REX₂EE motif [4].

NUDT5, Nudix hydrolase 9 (NUDT9), NUDT12 and NUDT14 are the human NUDIX enzymes with ADP-ribose (ADPR) pyrophosphatase activity [5]. Structural and sequence analysis identified NUDT9 as an evolutionary ancestor of all human NUDT enzymes [5]. It is mainly expressed in heart, skeletal muscle, liver, kidney and pancreas [6]. Two splice variants exist, one exhibits clear mitochondrial localization (due to an additional mitochondrial leader sequence), while the other was shown to be evenly distributed in the cell [7]. The NUDT9 crystal structure revealed a two-domain structure with the catalytic centre in the core of the monomeric protein [8], but a crystal structure in complex with ADPR is still missing. Apart from the characteristic NUDIX fold, NUDT9 reveals no structural homology to other NUDIX enzymes.

The C-terminal NUDT9-homology (NUDT9H) domain in the human transient receptor potential melastatin subfamily 2 (TRPM2) channel exhibits substantial sequence identity of 39% to NUDT9 [9]; TRPM2 conducts Na⁺, K⁺ and Ca²⁺ after activation by ADPR [9]. The NUDT9H domain is indispensable for TRPM2 gating [10–12], but a second ADPR binding site was recently identified in the N terminus of the channel [13,14]. Activation of TRPM2 after exposure of cells to oxidative stress is mediated by ADPR acting as a second messenger [11,15].

ADPR is a metabolite of the universal coenzyme nicotinamide adenine dinucleotide (NAD) that can be produced by the NAD-glycohydrolase CD38 [16]. In mitochondria, ADPR is released from mono-ADP-ribosylated proteins (reviewed in [17]). Alternatively, ADPR is released from poly-ADP-ribosylated proteins in the nucleus via the poly (ADP-ribose) glycohydrolase (reviewed in [18]). Another source of ADPR could be O-acetyl-ADPR produced by sirtuins [19,20].

In this study, we aimed to investigate the biophysical properties of NUDT9 in more detail to better understand its extraordinary specificity towards ADPR. We identified the ADPR derivative 2'-deoxy-ADPR as an additional substrate and analysed ligand-binding properties for both substrates using various biophysical methods. Further, we characterized the conformational changes upon ligand binding as well as the ligand-binding site using a combination of small-angle X-ray scattering (SAXS), NMR spectroscopy and molecular docking. These results open the path for a future adaptation of NUDT9 as an ADPR fluorescence resonance energy transfer (FRET) sensor.

Results and Discussion

2'-deoxy-ADPR is a substrate of the ADPR pyrophosphatase NUDT9

NUDT9 is the only enzyme of the human NUDIX hydrolase family with high substrate specificity. Out of more than 50 tested substrates, ADPR was the only one accepted by NUDT9 [5]. NUDT9 exhibits high substrate specificity towards ADPR, but high concentrations of 2'-phospho ADPR [21], O-Acetyl-ADPR [22] and inosine-diphosphate ribose (IDPR) [6,23] were also hydrolysed with reduced activity. A similarly high specificity is described for the ADPR-gated TRPM2 channel which contains a C-terminal domain homologous to NUDT9 [9]. Since the ADPR derivative 2'-deoxy-ADPR was identified as a TRPM2 agonist [24], we tested this as a substrate for NUDT9. We overexpressed NUDT9 (Glu59-Leu350, corresponding to the NUDT9 β transcript also used in [8]) in *Escherichia coli* and purified it using a C-terminal histidine tag by metal ion affinity chromatography. Indeed, 2'-deoxy-ADPR is hydrolysed to 2'-deoxy-AMP and ribose 5-phosphate; nucleotide hydrolysis and formation was detected by nucleotide HPLC analyses (Fig. 1A). K_M and v_{max} were determined for ADPR and 2'-deoxy-ADPR. K_M values for both substrates are comparable ($3.0 \pm 0.4 \mu\text{M}$ for ADPR vs $0.8 \pm 0.3 \mu\text{M}$ for 2'-deoxy-ADPR) but ADPR is turned over faster by NUDT9 as its v_{max} value of $42.2 \mu\text{mol}\cdot\text{min}^{-1}\cdot\text{mg}^{-1}$ is more than twice as high as $17.8 \mu\text{mol}\cdot\text{min}^{-1}\cdot\text{mg}^{-1}$ for 2'-deoxy-ADPR (Table 1). Previously reported K_M values for ADPR hydrolysis show considerable variation, ranging from 0.7 to 180 μM [6,9,22,25]. This might be due to additional AMP conversion by alkaline phosphatase and imprecise detection of inorganic phosphate mostly by colorimetric assays or insufficiently sensitive assays and calculation methods. Our data almost agree with the value of 0.7 μM reported by Carlotto *et al.* [25]. Our direct HPLC-based analysis of the products reduces inaccuracies in comparison to the additional use of alkaline phosphatase.

In order to determine the binding affinities, we performed isothermal titration calorimetry (ITC) analyses of NUDT9 and its substrates. Using Mg²⁺ as cofactor, the substrate hydrolysis was too fast and the produced heat of dilution too strong to detect binding. As Mn²⁺ facilitated partial activity of NUDT9 [7], we considered whether replacing Mg²⁺ by other divalent ions might allow ligand binding without hydrolysis. We found that replacing Mg²⁺ by Ca²⁺ prevents hydrolysis of ADPR or 2'-deoxy-ADPR, which allowed us to determine the high-affinity binding for both substrates

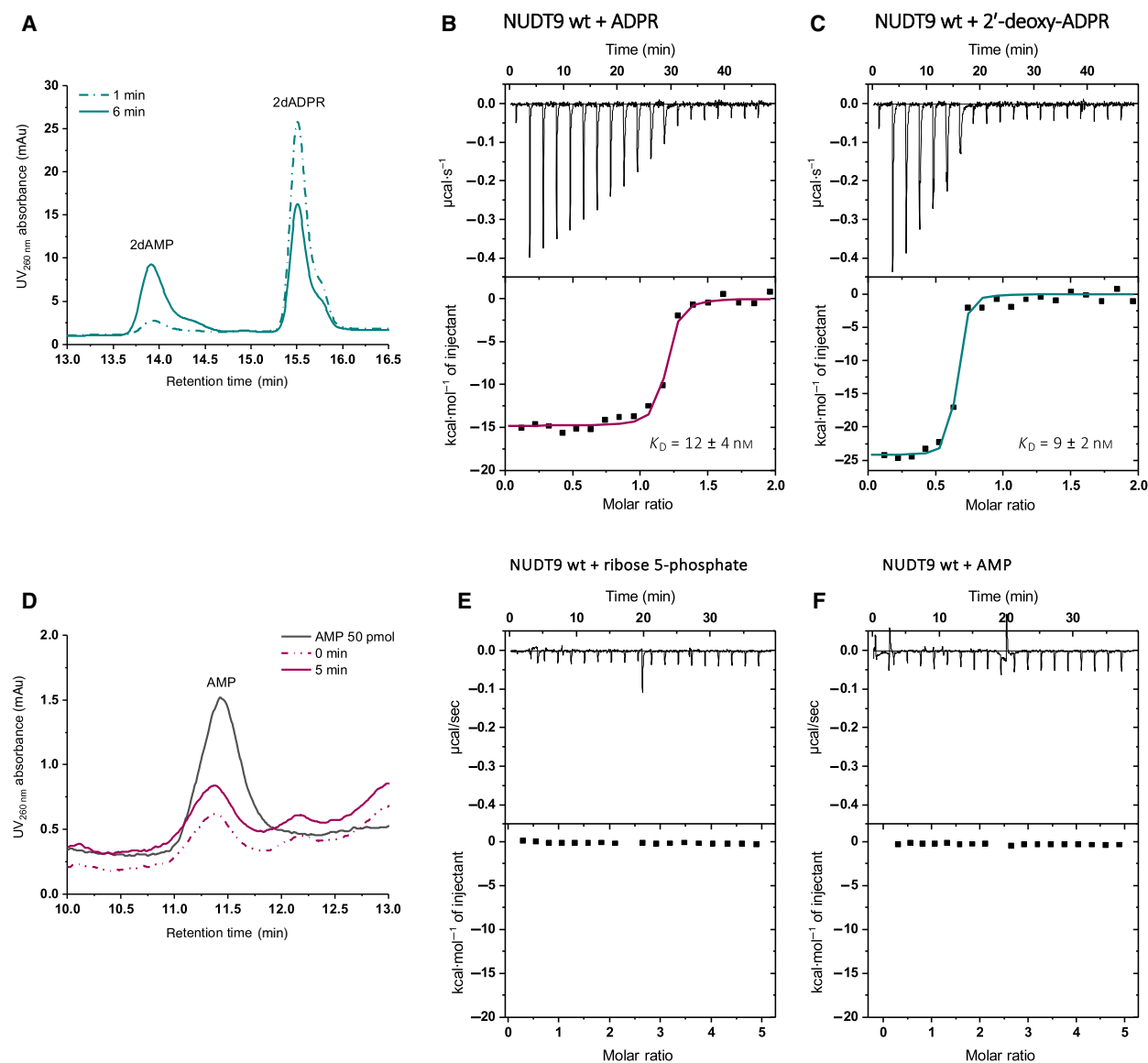


Fig. 1. 2'-deoxy-ADPR is an equivalent substrate for ADPR pyrophosphatase NUDT9. (A) 2'-deoxy-ADPR is hydrolysed by NUDT9 to 2'-deoxy-AMP and ribose 5-phosphate as quantified by HPLC analyses of the nucleotides. (B + C) Binding affinities of ADPR and 2'-deoxy-ADPR were determined by ITC using Ca^{2+} as cofactor that prevents substrate hydrolysis. ITC data were obtained from three individual experiments and presented as mean \pm SD, data were fitted using a one-site binding model. (B) Binding of ADPR to NUDT9 reveals a K_D of 12 ± 4 nM. (C) Binding of 2'-deoxy-ADPR to NUDT9 reveals a K_D of 9 ± 2 nM. (D) ADPR is not hydrolysed by NUDT9 using Ca^{2+} as cofactor. Less than 50 pmol AMP was formed out of 180 nmol ADPR after incubation with 100 ng NUDT9 at 37 °C. (E + F) ADPR breakdown products do not bind NUDT9. Ribose 5-phosphate (E) shows no binding to NUDT9 neither does AMP (F). All ITC measurements were performed at 20 °C.

Table 1. Kinetic and thermodynamic values for ADPR and 2'-deoxy-ADPR binding to NUDT9 are comparable. Using HPLC analysis of the hydrolysis, K_M and v_{\max} were calculated; values represent mean \pm SEM from 5 to 7 independent experiments. K_D , ΔH and ΔS were obtained by ITC using Ca^{2+} as cofactor. Values represent mean \pm SD from three independent experiments.

NUDT9 ligand	K_M ($\mu\text{mol}\cdot\text{L}^{-1}$)	v_{\max} ($\text{nmol}\cdot\text{min}^{-1}\cdot\mu\text{g}^{-1}\cdot\text{enzyme}$)	K_D (nM)	ΔH ($\text{cal}\cdot\text{mol}^{-1}$)	ΔS ($\text{cal}\cdot\text{mol}^{-1}\cdot\text{deg}^{-1}$)
ADPR	3.1 ± 0.4	42.4 ± 1.5	12 ± 4	-1528 ± 70	-16 ± 3
2dADPR	0.8 ± 0.3	17.8 ± 1.2	9 ± 2	-2415 ± 22	-46 ± 1

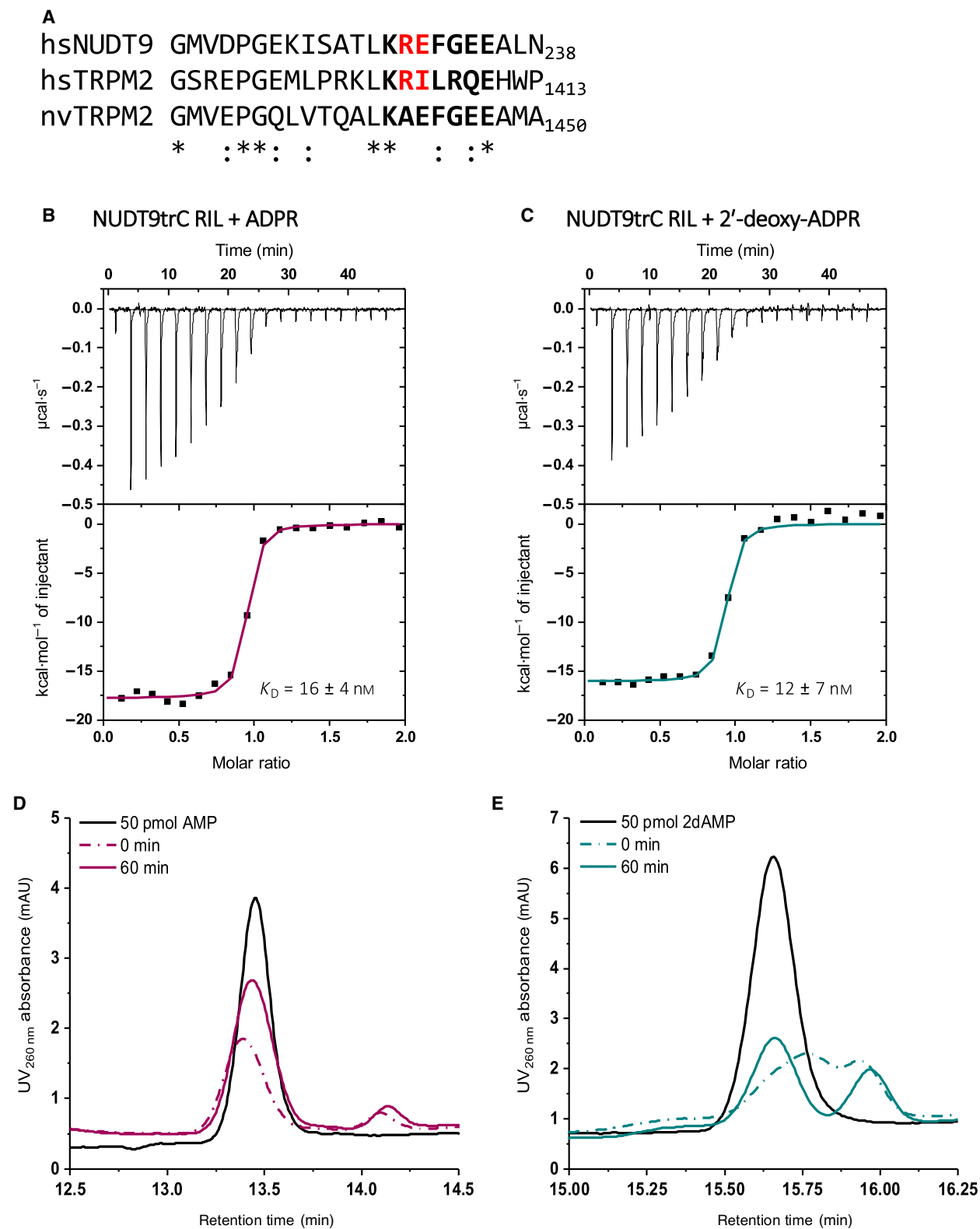


Fig. 2. Mutation in the NUDIX box (E230I F231L) preserves the NUDT9 binding affinity but inactivates the pyrophosphatase. (A) Sequence alignment of the NUDIX box from NUDT9, *hs*TRPM2 and *nv*TRPM2. Amino acid residues responsible for catalytic (in-)activity in NUDT9 and *hs*TRPM2 are coloured in red. (B + C) ITC measurements using Mg^{2+} as cofactor show a preserved nanomolar binding affinity for (B) ADPR and (C) 2'-deoxy-ADPR. Data were fitted using a one-site binding model. ITC data were obtained from three individual experiments and presented as mean \pm SD. (D + E) NUDT9 E230I F231L mutant does not hydrolyse neither ADPR (D) nor 2'-deoxy-ADPR (E).

(Fig. 1B–D) with similar K_D values of 12 ± 4 nM for ADPR and 9 ± 2 nM for 2'-deoxy-ADPR (Table 1). The enthalpy difference of $887 \text{ cal}\cdot\text{mol}^{-1}$ (Table 1) indicates an additional hydrogen bond most likely elicited by the different 2'-position of the two ligands. Although the crystal structure was solved for NUDT9 in complex with the ADPR break down product ribose 5-phosphate [8], we were unable to measure binding of ribose 5-phosphate or AMP by ITC (Fig. 1E,F).

While our measurements reveal similar binding affinities for ADPR or 2'-deoxy-ADPR to NUDT9, 2'-deoxy-ADPR was found to be a superagonist for TRPM2, inducing 10-fold higher whole-cell currents at saturation [24]. Whether this effect is caused by differences in binding affinities to the corresponding TRPM2 domains, variations in binding site preferences (NUDT9H vs. MHR1/2) or a combination thereof remains to be investigated.

Mutation in the NUDIX box (E230I/F231L) inactivates NUDT9 but preserves the ligand-binding affinity

The NUDIX boxes of NUDT9 and of the NUDT9H domain of *hs*TRPM2 show substantial differences: E230 and F231 in NUDT9 are replaced by I1405 and L1406 in *hs*NUDT9H (Fig. 2A). These substitutions were reported to be responsible for the loss of pyrophosphatase activity of *hs*NUDT9H, although the channel was initially described as a chanzyme [9]. Swapping the NUDT9 NUDIX box against the one from *hs*TRPM2 eliminated the pyrophosphatase activity of the enzyme [7], while the corresponding substitution of the *hs*TRPM2 NUDIX box prevented channel activation by ADPR [9,26]. TRPM2 from the sea anemone *Nematostella vectensis* (*nv*TRPM2) was found to be the evolutionary precursor of all contemporary TRPM2 channels [27]. Interestingly, human NUDT9 and *nv*NUDT9H reveal a higher sequence identity of 49% (vs 39% to the *hs*NUDT9H [9]), explaining the catalytic activity of the *nv*NUDT9H domain due to an intact NUDIX box in the catalytic centre [28,29] (Fig. 2A). In *hs*TRPM2, the NUDT9H domain is indispensable for channel gating but a *nv*TRPM2- Δ NUDT9H mutant is properly activated by ADPR [29]. These findings

implicated an additional ADPR binding site apart from the NUDT9H domain, later proven by several cryo-EM structures of TRPM2, that showed a second ADPR binding site in the N-terminal MHR1/2 domain [13,14,30]. These findings raised the question about the role of the NUDT9H domain in mammalian TRPM2 channels and whether ADPR could still bind to the mutated NUDIX box. We generated a NUDT9 variant with E230I and F231L substitutions in the NUDIX box and a truncated C terminus that corresponds to the C terminus of TRPM2 (E59-W339, named NUDT9trC RIL). Using ITC, we determined high-affinity binding of ADPR as well as 2'-deoxy-ADPR to this mutant (Fig. 2B,C) and calculated K_D values of 16 ± 4 nM for ADPR and 12 ± 7 nM for 2'-deoxy-ADPR. These results demonstrated that neither the mutations nor the cofactor (here we used Mg^{2+}) affect the binding affinity of NUDT9. As shown previously, the mutation efficiently prevented the hydrolysis of the substrates by NUDT9; < 50 pmol AMP or 2'-deoxy-AMP were generated within 1 h incubation at 37 °C (Fig. 2D,E).

ADPR and 2'-deoxy-ADPR bind to identical binding sites in NUDT9

So far, only subtle differences for ADPR and 2'-deoxy-ADPR binding to NUDT9 were detected. We used NMR spectroscopy to investigate whether both ligands bind to the same site in NUDT9. BEST-TROSY-NMR spectra of ^{15}N -labelled NUDT9trC RIL in complex with ADPR or 2'-deoxy-ADPR superimpose very well indicating identical binding sites for the two ligands in NUDT9 (Fig. 3A). This is not surprising as the only difference between the ligands is a missing oxygen atom at the 2'-position of the first ribose. Nevertheless, we identified five peaks with resonance shifts between the ADPR and 2'-deoxy-ADPR complex spectra (Fig. 3A, indicated by arrows). Triple-resonance experiments with perdeuterated ^2D , ^{13}C , ^{15}N -labelled protein allowed partial (85%) sequence specific backbone resonance assignment (Fig. 3B). We identified L161, R164 and D218 to be substantially shifted in ADPR compared to 2'-deoxy-ADPR binding. As these residues all are located in a defined region in between the two domains of NUDT9, we

Fig. 3. 2'-deoxy-ADPR and ADPR bind to identical sites in NUDT9 as determined by BEST-TROSY NMR. (A) TROSY spectra of the NUDT9/ADPR (red) and NUDT9/2'-deoxy-ADPR (blue) complexes are superimposed and show almost identical chemical shifts for most resonances; differences were indicated by arrows. (B) Backbone assignment of the NUDT9/ADPR complex enabled identification of ligand-responsive residues from (A), which are likely to be involved in ligand coordination.

used them as restraints for docking using HADDOCK [31]. The resulting model shows the adenosine group bound in a pocket between the two NUDT9 domains with the 2'-oxygen pointing towards the core of the protein. The terminal ribose is located in the same binding pocket as observed in the crystal structure of NUDT9 in complex with ribose 5-phosphate and Mg^{2+} [8] (Fig. 4). Interestingly, *ab initio* docking using AutoDock Vina [32] resulted in a very similar ligand-binding mode. The obtained ADPR binding pose is thus in agreement with the previous crystal structure with the ribose 5-phosphate fragment [8] as well as with our NMR results.

Substrate binding leads to closure of two domains and a more compact structure

Remarkably, the comparison of the BEST-TROSY NMR spectra of apo NUDT9trC RIL and in complex with ADPR revealed substantial differences (Fig. 5A). The overall number of peaks increased from the apo to the ligand-bound form and most peaks show substantial changes in chemical shifts indicating large conformational changes upon ligand binding. The loss of TROSY peaks for the apo sample is most likely caused by exchange broadening resulting from conformational exchange at an intermediate rate on the NMR timescale and indicate a ligand-dependent stabilization of the protein. We applied further biophysical techniques to structurally investigate the ligand-binding-induced changes in NUDT9.

Differential scanning fluorimetry (nDSF) monitors changes in the intrinsic tryptophan fluorescence of a protein that unfolds in an applied thermal gradient. Apo NUDT9trC RIL might unfold in two steps as indicated by two peak maxima in the nDSF profile (Fig. 5B). The NUDT9 crystal structure [8] clearly shows two domains: the C-terminal core domain containing the substrate binding pocket and the proteolytically labile N-terminal cap domain that enhances the ligand-binding affinity of the core [7,33]. The two nDSF peaks may reflect the individual unfolding of these two domains. Once the ligand is bound, NUDT9 is thermally stabilized and unfolds in a single step (Fig. 5B). No differences were detected between ADPR and 2'-deoxy-ADPR.

Small-angle X-ray scattering was used to obtain size and shape information of NUDT9 in its apo as well as

ligand-bound state in solution. Interparticle distances displayed by the $P(r)$ function describe the shape of the protein and reveal the maximum protein diameter. The maximum diameter of 8.0 nm for apo NUDT9 decreased to 7.2 nm once ADPR or 2'-deoxy-ADPR bound indicating a more compact conformation of the ligand-bound NUDT9 (Fig. 5C). The same trend could be seen in the Guinier analysis with radius of gyration values of 2.3 nm for NUDT9 and 2.2 nm for NUDT9/ADPR (data not shown). A similar more compact ligand-bound form caused by large movements of a single loop has been described for *E. coli* ADPRase, for which a cycling between open and closed conformation that preserves substrate specificity was proposed [34]. Comparison of our experimental SAXS data with the previous crystal structure of apo or ribose 5-phosphate and Mg^{2+} bound NUDT9 (pdb:1q33/1qvj) indicates that these structures are already adopting a compact, closed conformation (Fig. 5D), presumably caused by binding of the C-terminal tail in the binding pocket in the crystal packing [8].

Taken together, using different biophysical techniques, we discovered substantial conformational changes in NUDT9 induced by ligand binding that lead to a more compact and thermally stabilized protein.

Perspectives

NUDT9 can potentially be developed into an ADPR FRET sensor

The high substrate specificity together with the discovered substantial conformational changes occurring upon ligand binding inspired us to investigate whether NUDT9 can be developed into an ADPR fluorescence resonance energy transfer (FRET) sensor. This would allow *in vivo* observation of ADPR generation and signalling in cells, for example, in the case of oxidative stress. FRET sensors display conformational changes when energy is nonradiatively transferred from a donor to an acceptor molecule, which are at a discrete distance. We designed FRET experiments with NUDT9 via chemical labelling of individual side chains by small organic fluorescent dyes.

Cysteine labelling via maleimide click chemistry is highly specific [35] and allows the introduction of Alexa Fluor dyes, which are bright, photostable and insensitive to pH changes [36]. Before new cysteines were

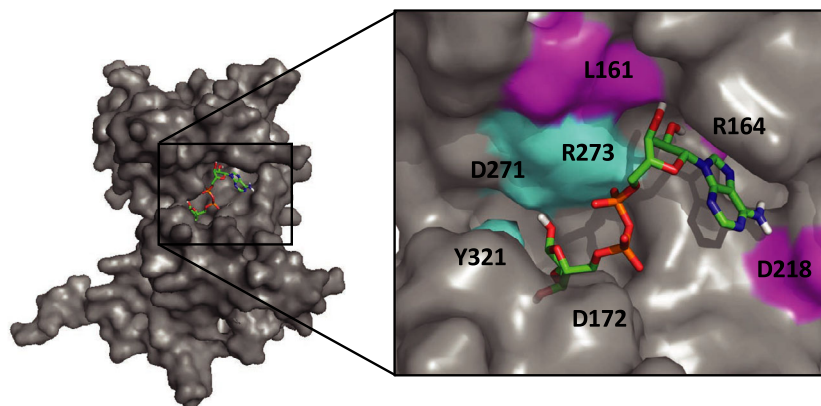


Fig. 4. Docking of ADPR into NUDT9. Model obtained from ambiguous interaction restraints docking using HADDOCK [31] with restraints from our NMR shifts (L161, R164, D218; magenta) as well as from the crystal structure of NUDT9 in complex with ribose 5-phosphate and Mg^{2+} (pdb:1qvj; D172, D271, R273, Y321; cyan). Residues showing significant chemical shift differences between ADPR and 2'-deoxy-ADPR are highlighted in magenta.

introduced into NUDT9trC RIL, the only inherent cysteine at position 207 was mutated to serine. ITC measurements confirmed the unchanged binding affinity of the NUDT9trC RIL C207S mutant (data not shown). All serine residues in NUDT9 were evaluated for their surface accessibility and distances to each other. Serine 78 and 118 in the cap and serine 182 in the core of NUDT9 (Fig. 6A) were mutated to cysteines by site-directed mutagenesis. A higher molecular weight and fluorescent band in the SDS/PAGE confirmed successful labelling by Alexa Fluor 555 and 594 (Fig. 6B). Strong FRET with an acceptor to donor ratio of 2.15 ± 0.53 was measured for apo NUDT9 labelled at positions 78 and 182; the ratio increased upon the addition of ADPR to 2.42 ± 0.68 (Fig. 6C). Moderate FRET with an acceptor to donor ratio of 0.90 ± 0.09 was measured for apo NUDT9 labelled at positions 118 and 182; the ratio decreased upon the addition of ADPR to 0.85 ± 0.10 (Fig. 6D). Ratio changes were calculated to $11.9 \pm 4.0\%$ (label positions 78 and 182) and $5.7 \pm 3.9\%$ (label positions 118 + 182). These results provide a general proof of principle of a FRET sensor for ADPR, which represents a starting point for further development. If these FRET sensors can be delivered into cells (e.g., via injection, electroporation or enclosed in vesicles [37]), we could envision developing a quantitative system for cellular ADPR concentration by modifying the binding affinity of the sensor.

Materials and Methods

Materials

All chemicals were of analytical quality and purchased from Carl Roth (Karlsruhe, Germany) or Sigma-Aldrich

(St. Louis, MO, USA), unless otherwise stated. 2'-deoxy-ADPR was purchased from Biolog Life Science Institute (Bremen, Germany).

Expression and purification of NUDT9

The pET51b(+) vector was used to express human NUDT9 with a C-terminal 10× histidine tag in *E. coli* B21 Gold cells. Protein expression was induced by IPTG and carried out overnight at 20 °C. Cells were lysed by pulsed sonication, and the cleared lysate was subjected to metal ion affinity chromatography. The C-terminally truncated version of NUDT9 contained an additional tobacco etch virus (TEV) cleavage site, which allowed the removal of the affinity tag. After an additional metal ion affinity chromatography to remove the TEV protease and the tag, proteins were finally purified by size exclusion chromatography. Protein purity was assessed by SDS/PAGE and their identity confirmed by mass spectrometry.

Site-directed mutagenesis

For all amino acid substitutions, site-directed mutagenesis was performed. Glutamate 230 and phenylalanine 231 were mutated to the corresponding TRPM2 residues isoleucine and leucine using the primer pair 5'-GATCTCTGCTACAT TAAAGCGTATTCTGGGTGAGGAGGCGTTGAACTC ATTACAG and 5'-CTGTAATGAGTTCAACGCCTCCT CACCCAGAATACGCTTTAATGTAGCAGAGATC. The following primer pairs were used for cysteine mutations: 5'-GGCGATCAAACGCAAAGACAGCGGCGAGTGGGC AATCCAGG and 5'-CCTGGGATTGCCACTCGCC GCTGTCTTTGCGTTTGATCGCC for C207S, 5'-GGGT CCAAAGTAGAGCGCTGCCAGGTCCTCAATGAGAA GG and 5'-CCTTCTCATTGGGGACCTGGCAGCGCTC TACTTTGGACCC for S78C, 5'-CCCACAAATCTCTGA

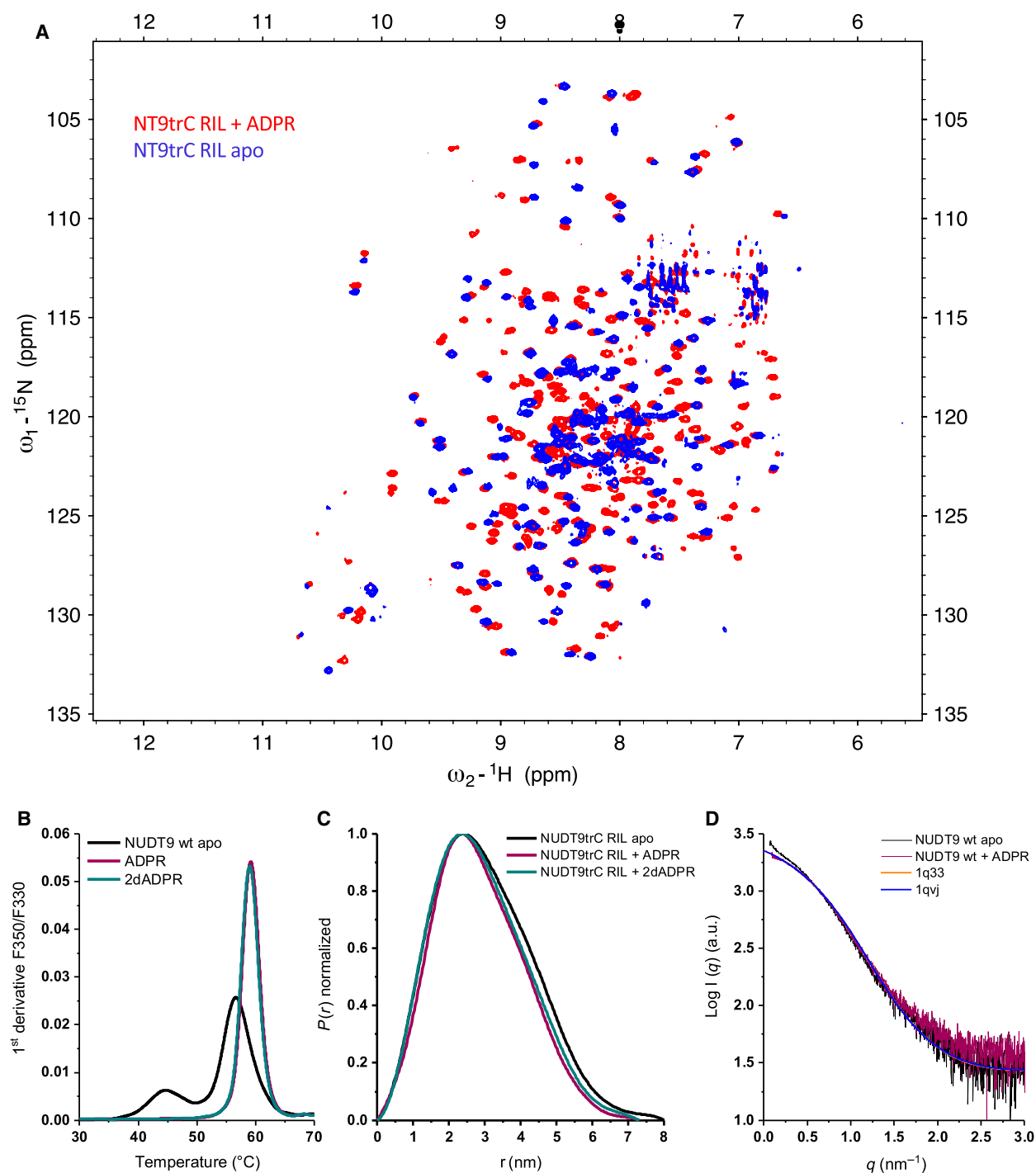


Fig. 5. Substrate binding leads to closure of two domains and a more compact structure of NUDT9. (A) BEST-TROSY NMR spectra show widespread chemical shift perturbation between apo NUDT9 (blue) and the NUDT9/ADPR complex (red), indicating substantial conformational changes upon ligand binding. (B) Apo NUDT9 unfolds consecutively (black), whereas the ligand-bound NUDT9 is stabilized and unfolds at once (purple for ADPR and green for 2'-deoxy-ADPR). (C) NUDT9 in complex with its ligands is more compact than apo NUDT9 as shown by SAXS. The $P(r)$ function reveals a D_{max} of 8.0 nm for apo NUDT9 compared to the substrate complex with a D_{max} of 7.2 nm. (D) Comparison of experimental SAXS data to calculated curves from the crystal structures of NUDT9 (pdb:1q33 and pdb:1qvj). The calculated curves obtained from the crystal structures of apo NUDT9 and in complex with ribose 5-phosphate and Mg^{2+} superimpose perfectly (blue and orange lines). Calculated curves reveal differences to the apo NUDT9 SAXS curve (black) in the low q range indicating differences in protein sizes, whereas calculated curves and experimental SAXS curves superimpose to a high degree indicating similar protein conformations for the NUDT9/ADPR complex (purple).

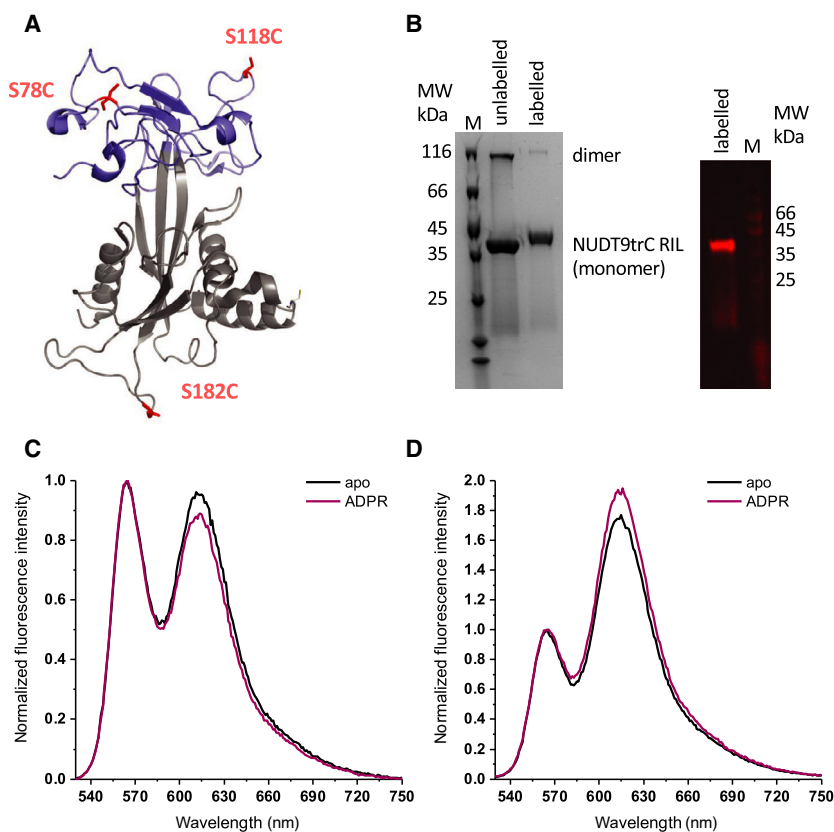


Fig. 6. NUDT9 can be developed into an ADPR FRET sensor. (A) Cartoon representation of NUDT9 with highlighted cysteine mutations in the cap (blue) and core domain (grey) of NUDT9 used for Alexa Fluor labelling by maleimide click chemistry. (B) SDS/PAGE of unlabelled and Alexa Fluor 555-labelled NUDT9 and in-gel fluorescence of labelled NUDT9. (C + D) Fluorescence measurements of NUDT9 labelled with Alexa Fluor 555 and 594 indicate changes in FRET upon ADPR binding. (C) NUDT9 labelled at positions 118 and 182 shows moderate FRET that decreases upon ADPR binding. (D) NUDT9 labelled at positions 78 and 182 shows strong FRET that increases upon ADPR binding.

GTGCAATTCAGTCCTAAATTTAACG and 5'-CGTTAAATTTAGGACTGAAATTCAGACTCAGAGATTTGTGG for S118C, and 5'-CACTCGTTGGAAGCGGATTTTCAGGGAACAAAATTATGCATCCGG and 5'-CCGGATGCATAATTTTGTTCCTGAACAATCGCGCTCCAACGAGTG for S182C. All clones were verified by nucleotide sequencing.

HPLC analysis of nucleotides

ADPR and 2'-deoxy-ADPR were hydrolysed by NUDT9 to AMP or 2'-deoxy-AMP and ribose 5-phosphate. For kinetic experiments, 0.3 ng wild-type NUDT9 was added to 0.3–30 μ M substrate and incubated for various amounts of time at 37 °C. For control experiments with mutated NUDT9 or with Ca^{2+} as cofactor, 10 ng NUDT9 was added to 100 μ M substrate and incubated for up to 1 h at 37 °C. Buffer conditions were 50 mM KH_2PO_4 (pH 7.2) supplemented by 2 mM MgCl_2 or CaCl_2 , respectively. All reactions were stopped by the addition of 1 mM KF [38] and freezing of the samples in liquid nitrogen. Methanol to a final concentration of 10% v/v was added to the filtered samples [Vivaspin 500 filter (MWCO 10 kDa; Sigma-Aldrich) removed the remaining protein] and then subjected to reversed-phase ion pair (RP-)HPLC analyses carried out on an Agilent 1260 infinity

module (Agilent Technologies, Santa Clara, CA, USA) as described previously [24]. Data acquisition and analysis were carried out using ChemStation Software (Agilent Technologies). The separation of the nucleotides was done on a Multohyp BDS C18 column (particle size 5 μ m, 250 \times 4.6 mm, Chromatographie Service, Langerwehe, Germany) applying an increasing methanol gradient [0 min (15%), 3.5 min (15%), 11 min (31.25%), 15 min (31.25%), 25 min (50%), 27 min (50%), 29 min (15%) and 38 min (15%)]. Nucleotides were detected at 260 nm using a Diode-Array detector (DAD; Agilent Technologies) and assigned and quantified using external standards.

Isothermal titration calorimetry

Binding assays were carried out on a MicroCal ITC-200 isothermal titration calorimeter (Malvern Panalytical, Malvern, UK). Proteins were dialysed in 20 mM HEPES pH 7.5, 150 mM NaCl and 5 mM CaCl_2 or MgCl_2 prior to the measurements; the ligands were dissolved in the respective buffer. Nineteen injections of 500–200 μ M of the respective ligand were titrated to 10 μ M protein provided in the cell. Each injection was interspaced by 150 s, and the stirring speed was set to 750 rpm. Ligand titrated into buffer allowed baseline correction. All measurements were

performed at 20 °C. The MicroCal Origin™ (Malvern Panalytical, Malvern, UK) program was used for data analysis, the binding curves were fitted by with a one-site binding model.

Differential scanning fluorimetry (nDSF)

Thermal protein unfolding was measured by differential fluorescence fluorimetry using a nanoDSF differential scanning fluorimeter (Prometheus, NanoTemper Technologies, Munich, Germany) that monitors intrinsic tryptophan fluorescence. NUDT9 and ADPR or 2'-deoxy-ADPR were diluted in 20 mM HEPES pH 7.5, 150 mM NaCl, 5 mM MgCl₂ to a final concentration of 10 μM protein and 750 μM ligand. A thermal gradient from 20 to 80 °C with a heating rate of 1 °C·min⁻¹ was applied. All measurements were performed in triplicates. The ratio was calculated from fluorescence intensities measured at 350 and 330 nm.

NMR spectroscopy

All NMR spectra were acquired on Bruker Avance III spectrometers equipped with an inverse detection cryogenic probe operating at 700 or 800 MHz ¹H frequency. All spectra were acquired in 20 mM HEPES (pH 7.5), 150 mM NaCl, 5 mM CaCl₂, 5% D₂O (v/v) except the pH control sample, which was acquired in 20 mM HEPES (pH 7.2), 150 mM NaCl, 5 mM CaCl₂, 5% D₂O (v/v). For binding studies, 800 MHz BEST-TROSY spectra [39] were acquired with a sample temperature of 293 K for 100–130 μM uniformly labelled ¹⁵N-NUDT9trC RIL alone or supplemented with 1 mM ADPR or 2'-deoxy-ADPR, respectively. The raw data matrix was 128 complex × 2048 points in *t*₁ and *t*₂, respectively, with an interscan relaxation delay of 0.6 s. A control experiment acquired with a small pH offset was used to identify TROSY peaks that are perturbed by small general changes to buffer conditions and may not necessarily be reflective of ligand-binding interactions. For backbone resonance assignment, TROSY-based 3D HN(CA)CO, HNCO, HNCA, HN(CO)CA, Cβ-optimized HNCACB and HN(CO)CACB spectra were acquired for 230 μM triple labelled ²D,¹³C,¹⁵N-NUDT9trC RIL at 700 MHz ¹H, 298 K. A non-TROSY (H)N(COCA)NH spectrum was also acquired for the same sample. All spectra were acquired with unmodified Bruker pulse programmes, processed with TOPSPKIN version 3.2 software (Bruker, Billerica, MA, USA) and analysed using NMRFAM-Sparky [40].

Alexa Fluor FRET labelling

Alexa Fluor labelling was conducted according to the manufacturer's instructions. Briefly, 50 μM purified protein was mixed with five-fold excess of each Alexa Fluor dye (10-fold excess of Alexa Fluor dyes in total) and incubated

overnight at 4 °C or for 2 h at room temperature. Unbound dye was consumed by the addition of 2 mM β-mercaptoethanol and removed using a PD-10 column. Absorbance spectra of the elution fractions were measured, and the amount of labelled protein was estimated. The labelling efficiency was almost 100% and unaffected by labelling at room temperature for 2 h or at 4 °C overnight. However, the ratio between the two bound fluorophores differed slightly within individual experiments.

Fluorescence spectroscopy

Fluorescence measurements were carried out on a Cary Eclipse Fluorescence Spectrometer (Agilent, Santa Clara, CA, USA). The scanning speed was 600 nm·min⁻¹, the slits were set to 5 nm, and PMT voltage was set to maximum of 800 Volts. Quartz cuvettes (Hellma Analytics, Müllheim, Germany) with a sample volume of 2000 μL were used. Alexa Fluor 555 donor was excited at 519 nm. Emission scans were acquired from 530 to 750 nm using 50 nm labelled NUDT9 alone or supplemented by 250 μM ADPR.

The ratio (*R*) and the changes were calculated according to the following equations:

$$R = \frac{\text{Intensity}_{\text{acceptor}}}{\text{Intensity}_{\text{donor}}}$$

$$\Delta R = R_{\text{max}} - R_{\text{min}}$$

and

$$R_{\text{change}} = \frac{\Delta R}{R_{\text{min}}}$$

Small-angle X-ray scattering

Small-angle X-ray scattering measurements were performed on the Bio-SAXS beamline P12 on the storage ring PETRA III (DESY, Hamburg, Germany). All measurements were carried out at room temperature in 20 mM HEPES (pH 7.5), 150 mM NaCl, 5 mM CaCl₂ or MgCl₂. 160 or 80 μM NUDT9trC RIL was measured alone or supplemented by 1 mM ADPR or 2'-deoxy-ADPR, respectively. Data averages were normalized and the background subtracted using automatic procedures on the beamline [41]. Forward scattering intensity of bovine serum albumin was used for calibration of the scattering intensity into absolute units of cm⁻¹. The scattering curves of all samples were buffer subtracted using the software PRIMUS [41] and the radii of gyration extracted by the Guinier approximation. Using the program GNOM [42], the distance distribution function (*P*(*r*)) and the maximal protein dimension (*D*_{max}) were calculated from the entire scattering curve.

Molecular docking

Restraint guided docking was performed using HADDOCK2.2 [8] with default parameters. The following restraints were used: L161, R164, D218 (from our NMR data) as well as D172, D271, R273, Y321 (from pdb:1qvj). *Ab initio* modelling was performed using AutoDock Vina [32] and default parameters.

Acknowledgements

We thank members of the Fliegert and Tidow laboratories for helpful discussions. The synchrotron SAXS data were collected at beamline P12 operated by EMBL Hamburg at the PETRA III storage ring (DESY, Hamburg, Germany). We acknowledge access to the Sample Preparation and Characterization (SPC) Facility of EMBL (Hamburg). This research was funded by the Collaborative Research Centre SFB1328 and the excellence cluster ‘The Hamburg Centre for Ultrafast Imaging - Structure, Dynamics and Control of Matter at the Atomic Scale’ of the Deutsche Forschungsgemeinschaft (DFG EXC 1074). This work was supported by the Medical Research Council, as part of United Kingdom Research and Innovation [MRC file reference number MC_U105184326]. [Correction added on 27 April 2022, after first online publication: the funding information has been updated in this version.]

Conflict of interest

The authors declares no conflict of interest.

Data accessibility

NMR assignment data have been deposited to the Biological Magnetic Resonance Data Bank (BMRB) with accession code 50870.

Author contributions

EG, TJR, FM, AB and SS involved in investigation; EG, RF and HT involved in writing; RF and HT involved in funding acquisition and supervision.

Peer Review

The peer review history for this article is available at <https://publons.com/publon/10.1111/febs.16097>.

References

- 1 McLennan AG (2006) The Nudix hydrolase superfamily. *Cell Mol Life Sci* **63**, 123–143.

- 2 Bessman MJ, Frick DN & O’Handley SF (1996) The MutT proteins or “Nudix” hydrolases, a family of versatile, widely distributed, “housecleaning” enzymes. *J Biol Chem* **271**, 25059–25062.
- 3 Gabelli SB, Bianchet MA, Bessman MJ & Amzel LM (2001) The structure of adp-ribose pyrophosphatase reveals the structural basis for the versatility of the nudix family. *Nat Struct Biol* **8**, 467–472.
- 4 Mildvan AS, Xia Z, Azurmendi HF, Saraswat V, Legler PM, Massiah MA, Gabelli SB, Bianchet MA, Kang LW & Amzel LM (2005) Structures and mechanisms of Nudix hydrolases. *Arch Biochem Biophys* **433**, 129–143.
- 5 Carreras-Puigvert J, Zitnik M, Jemth AS, Carter M, Unterlass JE, Hallström B, Loseva O, Karem Z, Calderón-Montanó JM, Lindskog C *et al.* (2017) A comprehensive structural, biochemical and biological profiling of the human NUDIX hydrolase family. *Nat Commun* **8**, 1541.
- 6 Lin S, Gasmi L, Xie Y, Ying K, Gu S, Wang Z, Jin H, Chao Y, Wu C, Zhou Z *et al.* (2002) Cloning, expression and characterisation of a human Nudix hydrolase specific for adenosine 5'-diphosphoribose (ADP-ribose). *Biochim Biophys Acta Protein Struct Mol Enzymol* **1594**, 127–135.
- 7 Perraud AL, Shen B, Dunn CA, Rippe K, Smith MK, Bessman MJ, Stoddard BL & Scharenberg AM (2003) NUDT9, a member of the Nudix hydrolase family, is an evolutionarily conserved mitochondrial ADP-ribose pyrophosphatase. *J Biol Chem* **278**, 1794–1801.
- 8 Shen BW, Perraud AL, Scharenberg A & Stoddard BL (2003) The crystal structure and mutational analysis of human NUDT9. *J Mol Biol* **332**, 385–398.
- 9 Perraud AL, Fleig A, Dunn CA, Bagley LA, Launay P, Schmitz C, Stokes AJ, Zhu Q, Bessman MJ, Penner R *et al.* (2001) ADP-ribose gating of the calcium-permeable LTRPC2 channel revealed by Nudix motif homology. *Nature* **411**, 595–599.
- 10 Wehage E, Eisfeld J, Heiner I, Jüngling E, Zitt C & Lückhoff A (2002) Activation of the cation channel long transient receptor potential channel 2 (LTRPC2) by hydrogen peroxide: a splice variant reveals a mode of activation independent of ADP-ribose. *J Biol Chem* **277**, 23150–23156.
- 11 Perraud AL, Takanishi CL, Shen B, Kang S, Smith MK, Schmitz C, Knowles HM, Ferraris D, Li W, Zhang J *et al.* (2005) Accumulation of free ADP-ribose from mitochondria mediates oxidative stress-induced gating of TRPM2 cation channels. *J Biol Chem* **280**, 6138–6148.
- 12 Fliegert R, Watt JM, Schöbel A, Rozewitz MD, Moreau C, Kirchberger T, Thomas MP, Sick W, Araujo AC, Harneit A *et al.* (2017) Ligand-induced activation of human TRPM2 requires the terminal ribose of ADPR and involves Arg1433 and Tyr1349. *Biochem J* **474**, 2159–2175.

- 13 Huang Y, Winkler PA, Sun W, Lü W & Du J (2018) Architecture of the TRPM2 channel and its activation mechanism by ADP-ribose and calcium. *Nature* **562**, 145–149.
- 14 Huang Y, Roth B, Lü W & Du J (2019) Ligand recognition and gating mechanism through three Ligand-binding sites of human TRPM2 channel. *Elife* **8**, 1–18.
- 15 Fonfria E, Marshall ICB, Benham CD, Boyfield I, Brown JD, Hill K, Hughes JP, Skaper SD & McNulty S (2004) TRPM2 channel opening in response to oxidative stress is dependent on activation of poly (ADP-ribose) polymerase. *Br J Pharmacol* **143**, 186–192.
- 16 Partida-Sanchez S, Gasser A, Fliegert R, Siebrands CC, Dammermann W, Shi G, Mousseau BJ, Sumoza-Toledo A, Bhagat H, Walseth TF *et al.* (2007) Chemotaxis of mouse bone marrow neutrophils and dendritic cells is controlled by ADP-ribose, the major product generated by the CD38 enzyme reaction. *J Immunol* **179**, 7827–7839.
- 17 Dölle C, Rack JGM & Ziegler M (2013) NAD and ADP-ribose metabolism in mitochondria. *FEBS J* **280**, 3530–3541.
- 18 Knowles H, Li Y & Perraud AL (2013) The TRPM2 ion channel, an oxidative stress and metabolic sensor regulating innate immunity and inflammation. *Immunol Res* **55**, 241–248.
- 19 Bauer I, Grozio A, Lasigliè D, Basile G, Sturla L, Magnone M, Sociali G, Soncini D, Caffa I, Poggi A *et al.* (2012) The NAD⁺-dependent histone deacetylase SIRT6 promotes cytokine production and migration in pancreatic cancer cells by regulating Ca²⁺ responses. *J Biol Chem* **287**, 40924–40937.
- 20 Hebert AS, Dittenhafer-Reed KE, Yu W, Bailey DJ, Selen ES, Boersma MD, Carson JJ, Tonelli M, Balloon AJ, Higbee AJ *et al.* (2013) Calorie restriction and SIRT3 trigger global reprogramming of the mitochondrial protein acetylome. *Mol Cell* **49**, 186–199.
- 21 Tóth B, Iordanov I & Csanády L (2015) Ruling out pyridine dinucleotides as true TRPM2 channel activators reveals novel direct agonist ADP-ribose-2'-phosphate. *J Gen Physiol* **145**, 419–430.
- 22 Rafty LA, Schmidt MT, Perraud AL, Scharenberg AM & Denu JM (2002) Analysis of O-acetyl-ADP-ribose as a target for nudix ADP-ribose hydrolases. *J Biol Chem* **277**, 47114–47122.
- 23 Kühn FJP, Watt JM, Potter BVL & Lückhoff A (2019) Different substrate specificities of the two ADPR binding sites in TRPM2 channels of *Nematostella vectensis* and the role of IDPR. *Sci Rep* **9**, 1–12.
- 24 Fliegert R, Bauche A, Wolf Pérez A-M, Watt JM, Rozewitz MD, Winzer R, Janus M, Gu F, Rosche A, Harneit A *et al.* (2017) 2'-Deoxyadenosine 5'-diphosphoribose is an endogenous TRPM2 superagonist. *Nat Chem Biol* **13**, 1036–1044.
- 25 Carloto A, Costas MJ, Comeselle JC, McLennan AG & Ribeiro JM (2006) The specific, submicromolar-Km ADP-ribose pyrophosphatase purified from human placenta is enzymically indistinguishable from recombinant NUDT9 protein, including a selectivity for Mn²⁺ as activating cation and increase in Km for ADP-ribose, both elicited by H₂O₂. *Biochim Biophys Acta Gen Subj* **1760**, 1545–1551.
- 26 Kühn FJP & Lückhoff A (2004) Sites of the NUDT9-H domain critical for ADP-ribose activation of the cation channel TRPM2. *J Biol Chem* **279**, 46431–46437.
- 27 Kühn FJP, Kühn C & Lückhoff A (2015) Functional characterisation of a TRPM2 orthologue from the sea anemone *Nematostella vectensis* in human cells. *Sci Rep* **5**, 8032.
- 28 Kühn F, Kühn C & Lückhoff A (2017) Different principles of ADP-ribose-mediated activation and opposite roles of the NUDT9 homology domain in the TRPM2 orthologs of man and sea anemone. *Front Physiol* **8**, 1–14.
- 29 Kühn FJP, Kühn C, Winking M, Hoffmann DC & Lückhoff A (2016) ADP-Ribose activates the trpm2 channel from the sea anemone *Nematostella vectensis* independently of the nudt9h domain. *PLoS One* **11**, 1–21.
- 30 Huang Y, Fliegert R, Guse AH, Lü W & Du J (2020) A structural overview of the ion channels of the TRPM family. *Cell Calcium* **85**, 102111.
- 31 Van Zundert GCP, Rodrigues JPGLM, Trellet M & Schmitz C (2016) The HADDOCK2.2 web server: user-friendly integrative modeling of biomolecular complexes. *J Mol Biol* **428**, 720–725.
- 32 Trott O & Olson AJ (2009) AutoDock Vina: Improving the speed and accuracy of docking with a new scoring function, efficient optimization, and multithreading. *J Comput Chem* **31**, 455–461.
- 33 Iordanov I, Mihályi C, Tóth B & Csanády L (2016) The proposed channel-enzyme transient receptor potential melastatin 2 does not possess ADP ribose hydrolase activity. *Elife* **5**, 1–20.
- 34 Gabelli SB, Bianchet MA, Ohnishi Y, Ichikawa Y, Bessman MJ & Amzel LM (2002) Mechanism of the *Escherichia coli* ADP-ribose pyrophosphatase, a Nudix hydrolase. *Biochemistry* **41**, 9279–9285.
- 35 Jansen LE, Negrón-Piñero LJ, Galarza S & Peyton SR (2018) Control of thiol-maleimide reaction kinetics in PEG hydrogel networks. *Acta Biomater* **70**, 120–128.
- 36 Panchuk-Voloshina N, Haugland RP, Bishop-Stewart J, Bhalgat MK, Millard PJ, Mao F, Leung WY & Haugland RP (1999) Alexa dyes, a series of new fluorescent dyes that yield exceptionally bright, photostable conjugates. *J Histochem Cytochem* **47**, 1179–1188.

- 37 Todorova R (2009) Estimation of methods of protein delivery into mammalian cells - a comparative study by electroporation and Biporter assay. *Appl Biochem Microbiol* **45**, 444–448.
- 38 McLennan AG (1999) The MutT motif family of nucleotide phosphohydrolases in man and human pathogens (Review). *Int J Mol Med* **4**, 79–89.
- 39 Lescop E, Schanda P & Brutscher B (2007) A set of BEST triple-resonance experiments for time-optimized protein resonance assignment. *J Magn Reson* **187**, 163–169.
- 40 Lee W, Tonelli M & Markley JL (2015) NMRFAM-SPARKY: Enhanced software for biomolecular NMR spectroscopy. *Bioinformatics* **31**, 1325–1327.
- 41 Konarev PV, Volkov VV, Sokolova AV, Koch MHJ & Svergun DI (2003) PRIMUS : a Windows PC-based system for small-angle scattering data analysis. *J Appl Crystallogr* **36**, 1277–1282.
- 42 Svergun DI (1992) Determination of the regularization parameter in indirect-transform methods using perceptual criteria. *J Appl Crystallogr* **25**, 495–503.